Cost-Effective and Wireless Portable Device for Rapid and Sensitive Quantification of Micro/Nanoplastics

Haoxin Ye[a], Xinzhe Zheng[b], Haoming Yang[a], Matthew D. Kowal[c], Teresa M. Seifried[c], Gurvendra Pal Singh[a], Krishna Aayush[a], Guang Gao[d], Edward Grant[c], David Kitts[a], Rickey Y. Yada[a], Tianxi Yang[a]*

a Food, Nutrition and Health, Faculty of Land and Food Systems, The University of British Columbia, Vancouver V6T1Z4, Canada

b Department of Computer Science, Faculty of Engineering, The University of Hong Kong, Hong Kong 999077, China

c Department of Chemistry, Faculty of Science, The University of British Columbia, Vancouver V6T1Z4, Canada

d Life Sciences Institute, The University of British Columbia, Vancouver V6T1Z2, Canada

*Corresponding author: Tianxi Yang (tianxi.yang@ubc.ca)

KEYWORDS: micro/nanoplastics, luminescent metal–phenolic networks, quantitative fluorescence imaging, on-site detection, wireless portable device

ABSTRACT: The accumulation of micro/nanoplastics (MNPs) in ecosystems poses tremendous environmental risks for terrestrial and aquatic organisms. Designing rapid, field-deployable, and sensitive devices for assessing the potential risks of MNPs pollution is critical. However, current techniques for MNPs detection have limited effectiveness. Here, we design a wireless portable device that allows rapid, sensitive, and on-site detection of MNPs, followed by remote data processing via machine learning algorithms for quantitative fluorescence imaging. We utilized a supramolecular labeling strategy, employing luminescent metal-phenolic networks composed of zirconium ions, tannic acid, and rhodamine B, to efficiently label various sizes of MNPs (e.g., 50 nm – 10 μm). Results showed that our device can quantify MNPs as low as 330 microplastics and 3.08×10^6 nanoplastics in less than 20 min. We demonstrated the applicability of the device to real-world samples through determination of MNPs released from plastic cups after hot water and flow induction, and nanoplastics in tap water. Moreover, the device is user-friendly and operative by untrained personnel to conduct data processing on APP remotely. The analytical platform integrating quantitative imaging, customized data processing, decision tree model and low-cost analysis ($0.015 per assay) has great potential for high-throughput screening of MNPs in agrifood and environmental systems.

Use of conventional plastics is abundant for many facets of contemporary life, including but not limited to applications for textiles, medical devices and food packaging materials.[1–3] However, the extensive use of plastics has led to substantial contamination of terrestrial and marine ecosystems. Of alarming concern is the fact that large visible plastic residues in the agri-food and environmental systems can interact with various substances that result in degradation to microplastics (MPs, particle size from 1 μm to 5 mm) and nanoplastics (NPs, particle size less than 1 μm) as a result of mechanical sheer stress, exposure to heat and ultraviolet (UV) photooxidation or microbial degradation.[4–6] These plastic fragments transport easily across food chains and water systems and pose health risks, including triggering oxidative stress, inflammation, and elevating death risks from specific diseases.[7–9]

Reliable detection of MNPs is critical for risk assessment analyses. Present-day methods for detecting and quantifying MNPs are suboptimal. Although imaging techniques, such as Transmission Electron Microscopy (TEM) and Confocal Laser Scanning Microscopy (CLSM) offer satisfactory visualization capability for MNPs, these techniques are lacking for quantitative analysis.[10–13] Alternative approaches, such as Particle Tracking Analysis (PTA) and Inductively Coupled Plasma–Mass Spectrometry (ICP-MS) are effective to determine MNPs concentrations; nonetheless, these methods also have limitations that include high cost of laboratory materials, time-consuming operations, and trained personnel to perform the analyses.[14–16] Additionally, the quantification of MNPs in diverse real-world plastic samples, including those derived from river , soil or released from commercial plastic packaging, presents considerable challenges. The rapidly advancing field of developing fluorescence-enabled portable microscopy presents a rapid and on-site imaging approach for specific analyte detection due to remarkable sensitivity and portability. Researchers have reported that fluorescence staining of microplastics is a promising method for fast recognition of plastic particles. For instance, Leonard et al.[17] developed a smartphone enabled device based on detecting microplastics utilizing Nile Red staining. However, this approach requires a 24-hour waiting period to mitigate unwanted background signal interference and also lacks the capability to identify nanoplastics specifically.[18] Moreover, Nile Red pH instability poses a further challenge to ensure assay accuracy, especially when analyzing environmental samples having diverse pH levels.[18]

In order to achieve rapid and accurate MNPs detection using a fluorescence-enabled method, a robust labeling method is needed. Metal phenolic networks (MPNs) are a class of

naturally derived low-toxic and stimulus-responsive metal–organic networks constructed from metal ions and phenolic ligands.[19–21] MPNs capture a variety of particle types (e.g., organic, inorganic, and biological entities) through the coordination between metal ions and phenolic ligands. Recently, MPNs have been integrated with organic dyes through π interactions that create various luminescent metal phenolic networks (L-MPNs) by a rapid and versatile coating process (< 5 min).[22] The outcome has demonstrated outstanding effectiveness in labeling diverse particles by producing ultra-thin coatings with tailored luminescence and exhibited stable fluorescence properties in various conditions (e.g., different pH environments, cell cytosol matrices).[22] Therefore, the utilization of L-MPNs as a labeling strategy provides great potential to enable fast and precise fluorescence detection of MNPs.

The use of portable devices for fluorescence detection of MNPs is an important consideration for convenient and on-site deployable detection. However, portable devices previously designed often necessitated specific smartphone models for integration, thus limiting factors such scalability, portability, and compatibility with other mobile pad or laptop devices. It is crucial to develop an analytical system that achieves both on-site and remote detection of plastic particles, considering the potential presence of plastic particles in inaccessible areas. Finally, it is equally important to create a user-friendly device that allows effective operation by untrained personnel and supports local or remote data processing for fast fluorescence imaging analysis.

This work describes our design of a wireless portable device that enables rapid, sensitive and on-site/remote detection of MNPs. We employed L-MPNs for labeling and concentrating MNPs, followed by detection and customized image processing via machine learning algorithms in a mobile device that supports quantitative fluorescence imaging analysis. This device described herein, offers a quick MNPs detection (< 20 min) with compatible data transmission with various mobile devices, such as smartphones, pads, and laptops through WIFI connection. The result is wireless communication and remote data processing up to a distance of 10 meters from mobile devices to the portable device. The user-friendly design of the device allows untrained personnel to process data effectively (Scheme 1). In this study, we selected tannic acid (TA), zirconium cation (Zr^{4+}), and rhodamine B (RhB) as model reagents to prepare L-MPNs. We utilized polystyrene (PS) particles of various sizes (10 μm, 1 μm, 500 nm, and 50 nm) to represent a wide range of plastic particle sizes found in known environmental situations. Our goal was to demonstrate high-performance of our assay, particularly in overcoming the challenges in visualizing plastic particles smaller than 10 μm, using traditional optical microscopy along with known difficulties related to nanoplastic detection. The TA/Zr^{4+} molar ratio was optimized for L-MPNs and the formation of MNPs labeled by L-MPNs (L-MPNs@MNPs) was validated by confocal fluorescence imaging. To demonstrate the feasibility of our device for on-site detection of real-world samples, we used the device to evaluate MNPs released from different commercial plastic cups after hot water and flow induction, and nanoplastics samples in tap water.

Scheme 1. Key attributes of the portable device for micro/nanoplastics detection. The microscope functions as a rapid, on-site detection apparatus for MNPs, with a detection time of less than 20 min. It offers compatibility with various mobile devices (e.g., smartphones, pads and laptops), enabling remote connections up to a distance of ~10 meters. A smartphone is presented as an example of a mobile device that can remotely process data acquired from the microscope efficiently, allowing for quantitively fluorescence imaging of MNPs. Data processing is user-friendly and can be executed by untrained personnel. Images in the Scheme are generated by Midjourney.

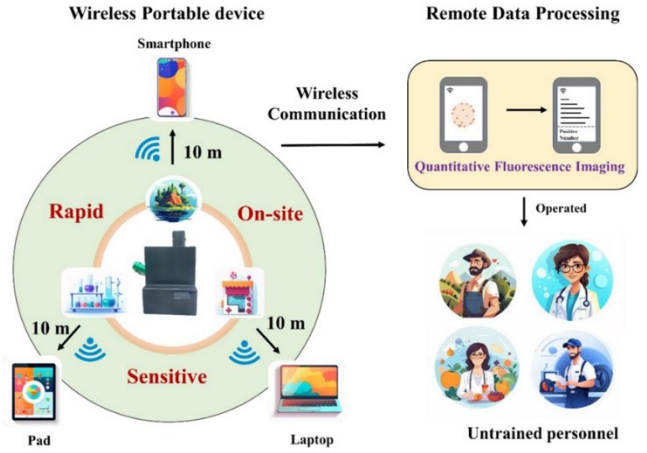

EXPERIMENTAL SECTION

Materials. Polystyrene micro-plastics and nano-plastics with four sizes (10 μm, 1 μm, 500 nm and 50 nm) were purchased from Phosphorex (Massachusetts, USA). Tannic acid (ACS reagent ≥99%), Rhodamine B (ACS reagent ≥99%), and zirconyl chloride octahydrate (ZrOCl2·8H2O, 98%) were purchased from VWR (Alberta, Canada). Commercial drinking cups consisting of polystyrene (PS), polypropylene (PP), polylactic acid (PLA) and polyethylene terephthalate (PET) were purchased from Amazon. A digital microscope was purchased from SKYBASIC (Houston, USA). Emission filter (550 nm, FWHM 33 nm, D25 mm) was purchased from Bock Optronics (Toronto, Canada) and Excitation filter (591.5 nm, FWHM 43 nm, D 12.5 mm) was purchased from Edmund Optics (Barrington, USA). A green LED Light was purchased from RaySoar (Jiaxing, China). Cellulose nitrate membrane filters were purchased from Fisher Scientific (Waltham, USA). Double distilled (DD) and tap water was obtained in Food, Nutrition and Health building at the University of British Columbia, and it was used throughout the experiment.

Preparation and Characterization of L-MPNs@MNPs. PS micro/nanospheres with various particle sizes (10 μm, 1 μm, 500 nm, and 50 nm) were diluted to obtain desired quantity concentration ranges. The standard procedure for preparing L-MPNs@MNPs was outlined below. 20 μL of TA (0.017 mM), 20 μL of RhB (0.5 mM), and 20 μL of $ZrOCl_2 \cdot 8H_2O$ (10 mM) were added into 940 μL of the aqueous MNPs suspension. The mixture was then vortexed for 60 s and was centrifuged at 7500 rpm for 10 min using a mini centrifuge (VWR, Alberta, Canada). After that, the supernatant was carefully removed and 100 μL of DD water was added to the original centrifuge tube. This was followed by transferring to a new centrifuge and was then vortexed for 60 s. Control group (L-MPNs solution) without adding MNPs was prepared using the same procedure as above. All experiments were repeated in triplicate. The characterization of L-MPNs was conducted by Dynamic Light Scattering (DLS) analysis, Zeta potential, fluorescence, Confocal Laser Scanning Microscopy (CLSM) and Electrophoretic Deposition (EPD)-Interferometric Scattering (iSCAT) measurements (Method S1).

Detection of MNPs by the Portable Device. L-MPNs labeling strategy was optimized prior to device operation (Method S2). 1 μL of the sample solution was deposited onto a square sample cell on gridded nitrocellulose membranes and allowed to evaporate naturally for 1 min. The prepared nitrocellulose substrates were then placed into the sample chamber of the portable device. Upon establishing the connection from a mobile device to the microscope via a WIFI hotspot, raw images (720 × 1280 pixels) were captured using the MAX-SEE software (Shenzhen Joyhonest Technology Co., Ltd) and analyzed utilizing a custom MATLAB code (Method S3) executed on the mobile device. Quantitative analysis of MNPs was detailed in Method S4.

Detection of MNPs in Real-world Scenarios. Three real-world scenarios were simulated to demonstrate the capability of the portable device for nanoplastics detection. Firstly, hot water-induced plastic release was studied by evaluating the MNPs released from six commercially available plastic cups consisting of PS, PP, PLA and PET. Prior to analysis, each cup was thoroughly washed with DD water to remove any potential contaminants that may have accumulated during the manufacturing, storage, transport, or unstacking process. 50 mL of heated DD water (100 °C) was then added to each plastic cup and allowed to cool down naturally for 30 min at room temperature. The PLA cup, which shrinks when exposed to hot water, was submerged in a beaker filled with 50 mL of boiling DD water (100 °C) followed by the same procedure as other cups. Secondly, flow-induced plastic release was conducted by measuring the MNPs release from PS cups pieces. A PS cup (7.27 g) was cut into pieces approximately 1 cm × 1 cm in size. These pieces were then immersed in 250 mL of DD water and subjected to stirring at 300 rpm for 24 h at room temperature. Thirdly, to simulate the presence of MNPs in a real environmental setting, 50 nm PS nanoplastics (1.10×10^{10} mL^{-1}) were spiked into tap water. After that, each plastic sample was analyzed by the portable device, fluorescence spectroscopy and DLS measurement. All experiments were repeated in triplicate.

RESULTS AND DISCUSSION

Labeling Mechanism of Micro/nanoplastics with L-MPNs. To accurately detect MNPs, we tested a mechanism of labeling MNPs with L-MPNs. The L-MPNs labeling strategy could be applied to plastic particles using a simple self-assembly process (Figure 1a).[23] The formation of L-MPNs altered the zeta potential of the plastic particles from -15.41 ± 0.42 to -20.16 ± 0.37 mV for 10 μm microplastics ($p < 0.0005$) and -15.63 ± 0.45 to -17.52 ± 0.73 mV for 50 nm nanoplastics ($p < 0.05$), respectively, due to deprotonation of TA,[22] (Figure 1b). When we used fluorescence to characterize RhB binding with 10 μm of microplastics (Figure 1c) and 50 nm of nanoplastics (Figure 1f), the results showed that relatively low fluorescence intensity occurred when MNPs were labeled with RhB, TA/RhB, and RhB/Zr^{4+} in comparison to L-MPNs ($p < 0.00001$). This outcome demonstrates the important role of coordination networks of L-MPNs for more efficient fluorescence labeling.[22] Comprehensive discussion for labeling mechanism can be found in Note S1. The Confocal Laser Scanning Microscopy (CLSM) images provided evidence of successful labeling of RhB onto the microplastics (Figure 1d) and nanoplastics (Figure 1g) through MPNs. Furthermore, Differential Interference Contrast (DIC) images clearly demonstrated the presence of a thin layer of L-MPNs on the surface of the microplastics (Figure 1e). In addition, cross-sectional CLSM images presented a stereoscopic representation of the impact of the L-MPNs on the MPs labeling (Figure S2), demonstrating a uniform labeling process. It was noteworthy that the NPs labeled by L-MPNs (L-MPNs@NPs) exhibited large clusters (Figure 1g and 1h), which supports a previous hypothesis that L-MPNs can facilitate the separation and concentrate nanoplastics via aggregation following traditional centrifugation.

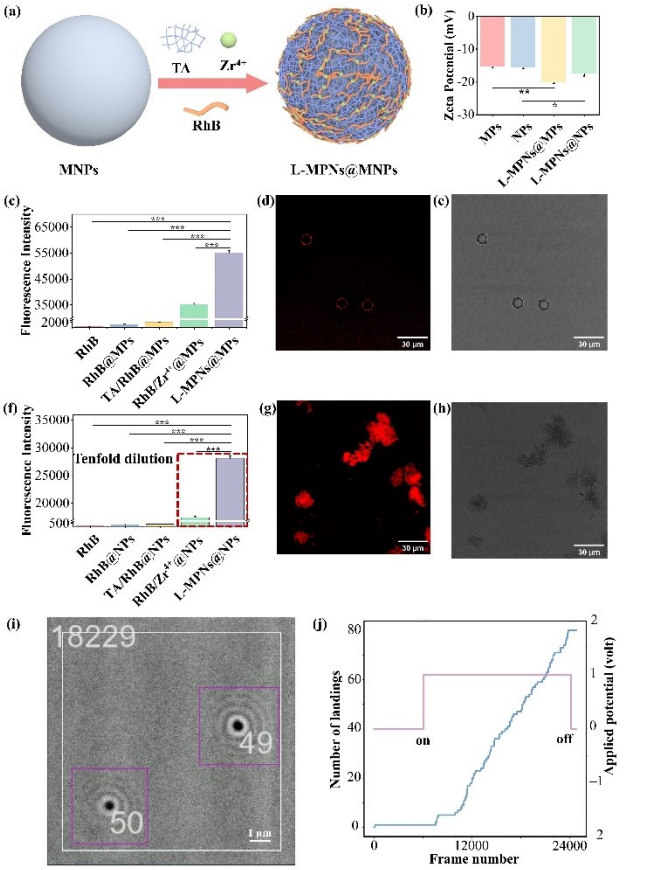

Figure 1. Labeling mechanism of L-MPNs for micro/nanoplastics. (a) Schematics of formation of L-MPNs@MNPs via self-assembly. (b) Changes in zeta potentials after formation of L-MPNs@MNPs. Effects of components from L-MPNs on formation of (c) L-MPNs@MPs and (f) L-MPNs@NPs illustrated via changes in fluorescence intensities, as determined by fluorescence spectroscopy. CLSM (d) and DIC (e) images of L-MPNs@MPs. CLSM (g) and DIC (h) images of L-MPNs@NPs. RhB/Zr^{4+}@NPs and L-MPNs@NPs solutions were diluted tenfold for the measurement of fluorescence intensity. (i) A frame extracted from particle tracking video recorded during iSCAT measurement, depicting nanoplastics in supernatant of L-MPNs@NPs solution after centrifugation. The upper left quadrant shows frame information (200 frames per second) and the particles are tracked within the designated region of interest (white box, 10.6 μm × 10.6 μm). (j) A plot delineating the variation in number of landings (blue line) and voltage status (pink line) over time during iSCAT measurement. 10 μm of MPs (8.78×10^5 mL^{-1}) and 50 nm of NPs (1.37×10^{13} mL^{-1}) were chosen as plastic particle representatives for all measurements except during iSCAT evaluations where 50 nm NPs were taken at a concentration of 1.37×10^{11} mL^{-1}. Data are represented as mean ± standard deviation (SD) of three technical replicates. *$p < 0.05$, **$p < 0.0005$, ***$p < 0.00001$ by two-tailed t test.

The efficiency of the separation process facilitated by the L-MPNs labeling method were measured a customized Electrophoretic Deposition (EPD)-Interferometric Scattering (iSCAT)

Microscope[24]. The particle tracking result from 50 nm PS NPs (0.227 nM) in the supernatant of L-MPNs@NPs solutions following centrifugation was shown in Figure 1i and the landing number over time was depicted in Figure 1j. The analysis and calculation of separation efficiency were detailed in Note S2. Consequently, the concentration of the sample supernatant was determined to be 6.22 ± 0.53 pM, culminating in a separation efficiency of 97.26 ± 0.23%. This performance is comparable to conventional coagulation/flocculation separation techniques for PS nanoplastics, which demonstrate a separation efficiency of 94.1%[25].

Design of Wireless Portable Device with Customized Data Processing. Concentrated L-MPNs@MNPs were used as target analytes to be detected by a wireless portable device with rapid and sensitive capabilities for on-site/remote quantification of MNPs. The device combined a mobile device, a digital microscope fitted with an emission filter, a green flashlight equipped with an excitation filter, a nitrocellulose membrane as sample substrates, a sample chamber, and a 3D-printed housing (Figure 2a). The actual appearance and compact size (approximately 11 cm* 9 cm*15 cm) of the device is presented in Figure 2b. Prototypes of the sample chamber and the 3D-printed housing are displayed in a disassembly view (Figure 2c) and a perspective view (Figure 2d). The rationale for the components selection was described in Note S3. The device provides remote detection capabilities within a range of approximately 10 meters (Figure 2a) and a sufficient field of view (FOV) with an effective pixel size of approximately 5.35 μm/pixel (Figure 2e). More details of the calculation supporting information are presented in Note S4 and Figure S3. The scale bar in each fluorescence image was presented as 500 μm according to the pixel count of approximately 93.46.

The entire process of image acquisition and analysis was streamlined using MAX-SEE software and a custom machine learning code in MATLAB executed on the smartphone mobile device. The image acquisition by the portable device is given in Video S1. As we moved the sample chamber, fluorescent signals (orange circle) consistently appeared on the smartphone screen, indicating the presence of MNPs. Remarkably, the sample chamber had the capacity to accommodate dozens of samples, and the device allowed for rapid image acquisition (less than 5 seconds per sample). This demonstrated the potential for high throughput detection. The principal goal of the imaging analysis was to translate the fluorescent signal from raw images into pixel areas and established the relationship between pixel area and known quantities of MNPs with varying sizes nanoparticles (e.g., 10 μm, 1 μm, 500 nm and 50 nm) for obtaining pre-training dataset for quantitative analysis of MNPs. The imaging process consists of several steps (Figure 2f): (1) extraction and demosaicing of the red channel of each RGB image to produce a grayscale image; (2) application of a threshold intensity of +25 to eliminate background noise and subsequent image binarization; (3) determination of the MNPs quantities, based on the known relationship between MNPs quantities and pixel areas. The determination of threshold intensity was previously discussed into assay optimization section. The output results are shown in Figure 2f and Figure S4 which included: (i) a positive or negative signal indicating if MNPs are present (Note that the value below the LOD is considered negative in this study); (ii) quantity concentration of plastic particles assuming a specific particle size (10 μm, 1 μm, 500 nm and 50 nm); and (iii) notification of dilution is required (If the quantity concentration is higher than the upper Limit of Quantification (LOQ), a dilution request is shown (Figure S4a)).

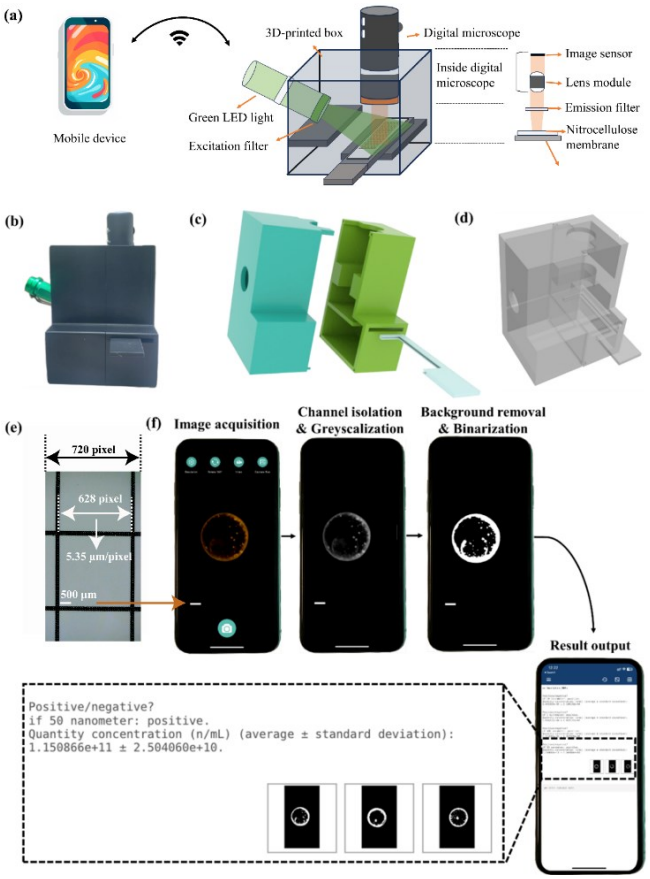

Figure 2. (a) Schematic presentation of the wireless portable device highlighting the illumination and image acquisition components. (b) Actual appearance of the device. Depiction of the 3D-printed box prototype: (c) view with disassembly, (d) view with assembly and perspective. (e) Raw image (1280 × 720 pixels) of a gridded nitrocellulose membrane captured using the device under white light. The scale bar 500 μm was determined based on a known pixel length (628 pixels) and known side length (3.36 mm) of a gridded square unit, resulting in a resolution of 5.35 μm/pixel. (f) Image processing steps and output results of fluorescence image in the device. 50 nm of nano-plastics (1.10×10^{11} mL^{-1}) labeled by L-MPNs (TA, 0.34 μM, RhB, 0.01 mM, Zr^{4+}, 0.20 mM) are chosen as the exemplary sample.

Assay Optimization for Reliable Detection. The optimization of the device and the assay used to minimize interference is important to achieve reliable and accurate detection of MPNs. In this study, we focused on optimizing TA/Zr^{4+} molar ratio in the self-assembled L-MPNs, because this ratio could influence the quantity of unwanted precipitates (L-MPNs alone without labeled onto MNPs), potentially causing excessive background noise when examined by the device. Additionally, this ratio could also influence the binding affinity of RhB to MPNs, thus impacting the resultant fluorescence signals.[26,27]

To optimize the TA/Zr^{4+} molar ratio, we evaluated the fluorescence performance of precipitated L-MPNs using traditional fluorescence spectroscopy (Figure S5) and fluorescence microscopic images via the designed portable device (Figure 3a). The final concentration of Zr^{4+} in all sample solutions was kept constant at 0.20 mM, a value identified to be appropriate from previous studies.[28] As demonstrated in Figure S5a, the precipitate of L-MPNs did not exhibit substantial visual changes initially but gradually diminished as the TA/Zr^{4+} molar ratio decreased from 1:30 to 0:1 after centrifugation. At high TA/Zr^{4+} molar

ratios ranging from 3:1 to 1:1, the precipitate formed large aggregates that could incorporate significant amounts of RhB. This result produced low fluorescence intensity (Figure S5b), possibly attributed to aggregation-induced fluorescence quenching.[29] Conversely, this phenomenon was found to be less pronounced as the TA/Zr^{4+} molar ratio was reduced from 1:1 to 1:30; leading to an increase in the fluorescence intensity. Further reduction of the TA/Zr^{4+} molar ratio (from 1:30 to 0:1) led to a reduction of the L-MPNs precipitate, as evidenced by a change in fluorescence intensity from 33211 ± 734 to 649 ± 31 (Figure S5b). This indicated that the amount of TA has an important role in producing the fluorescence intensity of precipitated L- MPNs.[30,31]

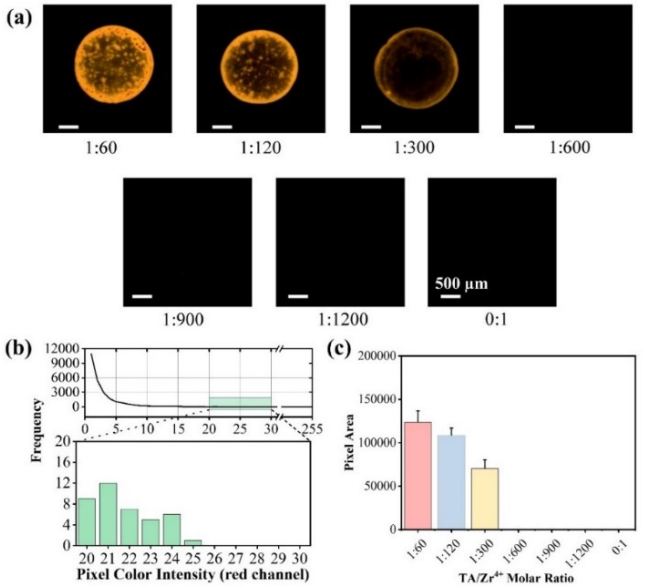

Figure 3. Assay optimization for L-MPNs using the designed portable device. Zr^{4+} concentration was selected as 0.20 mM. (a) Microscopic fluorescence images obtained from the portable device depicting L-MPNs precipitates with varied TA/Zr^{4+} molar ratios ranging from 1:60 to 0.1. All raw images are cropped to 600 × 600 pixels in regions exhibiting fluorescent signals and scale bar is 500 um. (b) Frequency distribution of red pixel color intensities for L-MPNs precipitates at a TA/Zr^{4+} molar ratio of 1:600. (c) Pixel area signals derived from fluorescence microscopic images of L-MPNs precipitates at TA/Zr^{4+} molar ratios from 1:60 to 0.1. Data are represented as mean ± SD of three technical replicates in Figure c.

Optimal TA/Zr^{4+} molar ratios are required since it would be expected that a high ratio could produce high background noise corresponding high pixel area values, whereas small ratios could weaken the binding of RhB to MPNs for labeling of plastic particles. We determined an optimal TA/Zr^{4+} molar ratio using systemic analysis of fluorescence microscopic images. A molar ratio lower than 1:600 produced no orange color in microscopic images (Figure 3a), but when standardized to 1:600, the frequency of red pixel intensities was increased at low red pixel intensities (< +5), and a maximal red pixel intensity of +25 (Figure 3b). To remove possible interference deriving from L-MPNs that remained uncapped onto MNPs, a threshold intensity of +25 was used to effectively eliminate background noise. Settimg this threshold showed no detectable pixel area signals at TA/Zr^{4+} molar ratio of lower than 1:600 (Figure 3c). A TA/Zr^{4+} molar ratio of 1:600 was the optimal ratio used along with threshold intensity of +25 to deduct background in the microscopic image.

Quantification of MNPs. Following optimization of the assay, the relationship between pixel area signals and MNPs concentrations for quantitative analysis was established. This relationship was critical to assure an accurate analysis of MNPs. We determined the upper and lower limit of quantification (LOQ) of MNPs using the portable device and formed a pretraining dataset for detecting unknown plastic samples.

The LOQ of MNPs was based on the quantity number of plastic particles, rather than sample concentration since MNPs were detected after centrifugation, and the sample volume before centrifugation may vary and thus influenced the concentration of separated MNPs. Microscopic images of various quantities of plastic particles with different sizes of 50 nm, 10 μm, 1 μm, 500 nm are shown in Figure S6–S9, respectively. Increasing MNPs produced two distinct phases in change of pixel area: a linear ascending phase (Phase 1) and a plateau phase (Phase 2) (Figure 4a–4d). Measured pixel area was linearly correlated ($R > 0.95$) with sample MNPs content, for both micro- and nano-sized plastic particles (Figure 4e–4h), demonstrating feasibility for the portable device to perform quantitative analysis. The LOQ of the portable device was determined at both upper and lower boundaries of Phase 1 using an iterative algorithm, whereby the mean and deviation were calculated to assess whether a higher quantity of plastic particles fell within a linear ascending phase (Method S5). Exceeding the upper LOQ, typically indicates that an increase in aggregation of MNPs occurred which lead to inaccurate results.[17] For example, the degree of aggregation of L-MPNs@NPs (50 nm) increased as the NPs quantity increased (Figure S10). When the NPs quantity exceeded an upper LOQ (Figure S10a–S10b), numerous large aggregates with size over 5 μm were observed, resulting in a saturated fluorescent signal in all NPs sample regions on nitrocellulose substrates (Figure S9). This in effect resulted in inaccuracy to quantity of NPs. The lower LOQ was established by progressively reducing the quantities of MNPs until minimal fluorescent signals were detectable. As shown in Figure S6–S9, respectively, negligible fluorescence signals occurred for MNPs when the quantities were less than 330 for 10 μm MPs; 2.1×10^5 for 1 μm MPs; 3.08×10^6 for 500 nm NPs; 2.58×10^8 for 50 nm NPs, respectively. Additionally, the pixel area corresponding to MNPs quantities below the lower LOQ showed values greatly beneath the pixel area signals of LOQ (< 150) (Figure S11a–S11d). Such ultralow signals cannot be recognized as plastic signals, confirming that the LOD of this assay was equal to the lower LOQ. This phenomenon aligned with reported smartphones-enabled fluorescence techniques.[22,25,45] Moreover, the comparison of the portable device with fluorescence spectroscopy revealed a superior reliability and sensitivity of the device for MNPs quantification (Note S5).

Analysis of MNPs in Real-world Scenarios. To further demonstrate the feasibility of using our device for analysis of plastic contaminations in real-world environmental settings, we detected plastics in three real-world scenarios: 1) Hot water-induced release of plastics from commercial drinking cups; 2) Flow-induced release of plastics in environmental water system; 3) Spiked plastics in tap water (50 nm PS, 1.10×10^{11} mL^{-1}) (Figure 5a). Figure S13a–S13b show that the fluorescence intensity of plastic samples corresponded to the pixel area obtained by the portable device, ensuring accurate fluorescence detection. Due to the fact that the released plastic samples may contain a wide size range of plastic particles,[32] the selection of an appropriate linear curve was critical for the precise quantification of MNPs. To determine the suitable linear curve used for

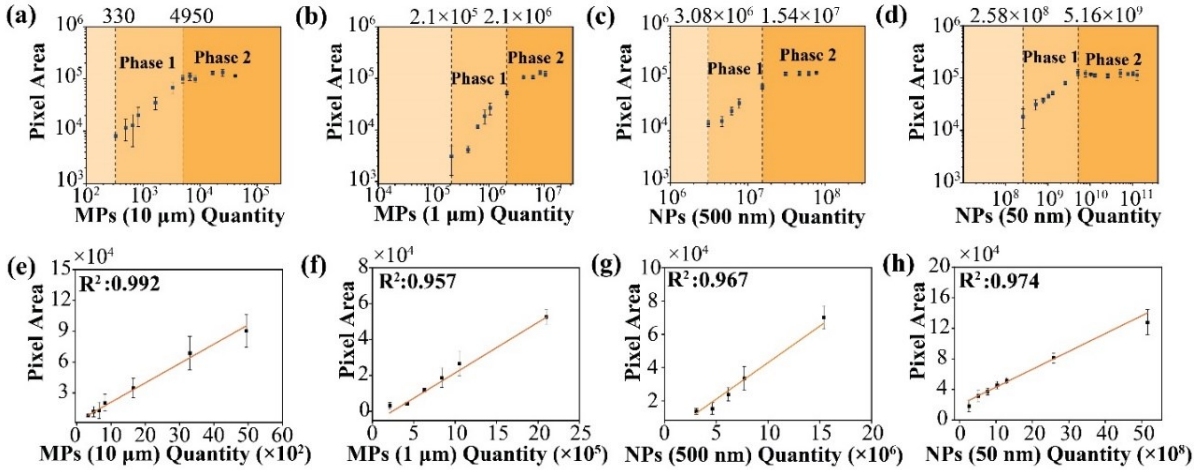

Figure 4. Comparison of the portable device with fluorescence spectroscopy for MNPs quantification. Relationship between pixel area detected by the portable device and MNPs quantities with particle sizes of 10 μm (a), 1 μm (b), 500 nm (c) and 50 nm (d). Linear relationship of pixel area as a function of MNPs quantities with particle sizes of 10 μm (e), 1 μm (f), 500 nm (g) and 50 nm (h) determined by the portable device ($p < 0.000001$ by ANOVA analysis for all groups). The tested quantity concentration ranges are 17553 – 4.39×10^6 mL^{-1} for 10 μm MPs, 2.23×10^6 – 1.12×10^9 mL^{-1} for 1 μm MPs, 1.64×10^7 – 8.19×10^9 mL^{-1} for 500 nm NPs and 2.74×10^9 – 1.37×10^{13} mL^{-1} for 50 nm NPs. Data are represented as mean ± SD of three technical replicates.

accurate quantification, we used Dynamic Light Scattering (DLS) techniques to analyze the particle size distribution of released MNPs in hot water and flow induction (Figure S14). The released MNPs showed a relatively homogeneous particle size distribution between 300 nm and 900 nm. This result was consistent with other studies where the plastic particles released from common single-use consumer plastic products under hot water and flow induction were concentrated in a nanometer size range.[14,33] We quantified five PS samples using the established linear curve as shown in Figure 4. According to our DLS results, the fitting standard curve for 1 μm particles was applied to PS1, while the curve for 500 nm particles was utilized for PS2, PS3 and PS4. This was attributed to the fact that PS1, PS2, PS3 and PS4 particles exhibited the strongest particle size peaks at 879 nm, 636 nm, 391 nm and 424 nm, respectively. As for nanoplastics spiked in tap water (PS5), 50 nm particles fitting curve was applied. To further refine MNPs quantity analysis, , a comprehensive decision tree model was established for analyzing MNPs across diverse samples from agri-food or environmental systems (Note S6 and Figure 5c).

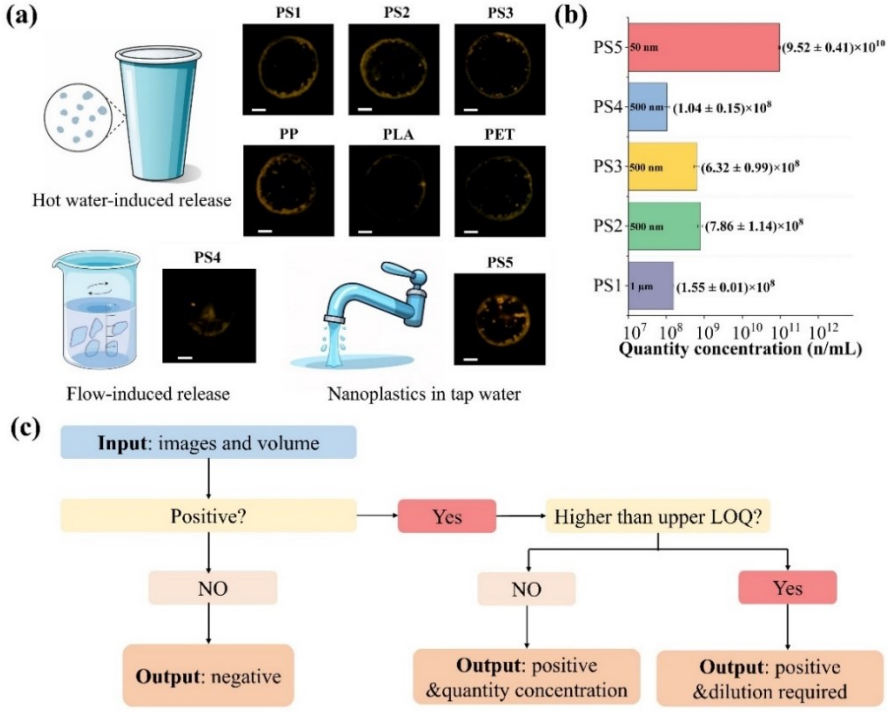

Figure 5. Assessment of plastic release from six types of commercial cups made from PS, PP, PLA, and PET. (a) Diagram showing plastic detection in three real-world scenarios and corresponding fluorescence microscopic images of the plastic particles obtained using the portable device. All raw images are cropped to 600 × 600 pixels in regions exhibiting fluorescent signals. Error bar is 500 μm. (b) Assay results for PS plastic particles in three scenarios by the portable device. (c) Decision Tree Model illustrating the detection and quantification process for plastic particles from unknown samples. Scenario 1 is hot water-induced release of plastics from following commercial drinking cups: PS1, Polystyrene opaque cups; PS2, Polystyrene foam cups; PS3, Polystyrene clear cups; PP, Polypropylene cups; PLA, Polylactic acid

cups; and PET, Polyethylene terephthalate cups. Scenario 2 is flow-induced release of plastics in environmental water systems (PS4, plastic pieces from polystyrene clear cups). Scenario 3 is spiked nanoplastics in tap water (PS5, 50 nm PS, 1.10×10^{10} mL^{-1}). Data are represented as mean ± SD of three technical replicates in bar charts.

Using this protocol, we showed that five PS samples gave positive signals and pixel areas that were within the linear curve range, and concentration of particles was determined in Figure 5b. Results from PS1-PS3 were consistent with other studies that reported plastic packaging could release hundred-million levels of plastic fragments in hot water.[14] PS4 is used to simulate the MNPs release from plastic products when in lakes or oceans under natural currents. After 24 h of flow induction, released nanoplastics were measured and the nanoplastic concentration also reached hundreds-millions levels with a plastic-to-DD water exposure ratio of 29.1 mg/mL. Nanoplastics spiked in tap water showed a good recovery ratio of 86.51 ± 3.4 % by comparing the determined and original concentrations. These results showcase the strong applicability of the device for practical environmental applications in pure real-world scenarios.

To highlight the merits of our assay, we conducted a comparative assessment of our portable device for nano-plastic analysis against recently established methods, considering factors such as nano-plastic types, pretreatment, LOD, and detection time (Note S7 and Table S2). Our device to quantify plastic particles has distinct advantages that include the following features: (1) the deployment of a highly-efficient labeling strategy utilizing L-MPNs to enable rapid detection of micro/nanoplastics; (2) the development of a multi-compatible portable device with wireless communication capabilities, allowing on-site and remote detection; (3) the requirement for minimal sample pretreatment, low sample volume (1 μL), and low-cost sample analysis (approximately $0.015/sample, Table S2); (4) user-friendly data processing. While our approach currently applies only to purified plastic samples, it holds the potential for broader application in real-world, complex systems, provided that these systems undergo effective separation and purification processes. Our platform can be extended to detect various particle analytes without inherent fluorescence through simple L-MPNs supramolecular labeling strategy, an innovation that will pave the way toward for high-throughput and rapid assay in diverse agri-food or environmental systems.

CONCLUSIONS

In summary, a novel wireless portable device was developed for rapid, sensitive and on-site quantification of diverse sizes (10 μm, 1 μm, 500 nm, and 50 nm) of MNPs. L-MPNs constructed from zirconium ions, tannic acid, and rhodamine B were employed to functionalize MNPs for fluorescence labeling and MNPs separation. The formation of L-MPNs@MNPs was confirmed by fluorescence spectrometer, zeta potential measurements, CLSM, and DIC imaging. The effective quantification of MPNs was achieved by customized fluorescence image processing on a mobile device app with machine learning algorithms. A customized Decision Tree Model embedded in the app was designed for decision-making and rapid quantitative analysis of MNPs. We demonstrated that the device allowed the detection of plastic numbers as low as 330 for 10 μm MPs, 2.1×10^5 for 1 μm MPs, 3.08×10^6 for 500 nm NPs and 2.58×10^8 for 50 nm NP. The analysis of MNPs released from six commercially available cups composed of PS, PP, PLA, and PET were also validated using the device. This analytical platform exhibited rapid detection (approximately 20 minutes), wireless data communication, remote data processing, high-efficient data management, low cost for device and assay, and high sensitivity comparable to previously established methods. This approach has the potential to serve as a preliminary assessment tool for early detection of MNPs in real-world samples, facilitating the accurate assessment of potential risks MNPs pose to both terrestrial and aquatic organisms and ultimately contributing to the safety and sustainability of ecosystems.

ASSOCIATED CONTENT

Supporting Information

The Supporting Information is available free of charge on the ACS Publications website.

Methods for EPD-iSCAT measurements, optimization, image processing, quantitative analysis and determination of upper LOQ; notes for labeling mechanism, determination of separation efficiency, device design and comprehensive assessment (PDF)

Movie of assay procedure for micro/nanoplastics using the portable device (MP4)

AUTHOR INFORMATION

Corresponding Author

*E-mail:tianxi.yang@ubc.ca

Present Addresses

Food, Nutrition and Health, Faculty of Land and Food Systems, The University of British Columbia, 2205 East Mall, Vancouver BC, V6T 1Z4 Canada.

Author Contributions

The manuscript was written through contributions of all authors. All authors have given approval to the final version of the manuscript.

Notes

The authors declare no competing financial interest.

ACKNOWLEDGMENT

This work was supported by the UBC Faculty of Land and Food Systems/Start Up Funds (AWD-020249 UBCLANDF 2022), Natural Sciences and Engineering Research Council of Canada (NSERC) Discovery Grants Program (RGPIN-2023-04100, RYY RGPIN 04598) and NSERC Discovery Grants Program-Discovery Launch Supplement (DGECR-2023-00386). Imaging was performed in the LSI Imaging Core Facility of the Life Sciences Institute at the University of British Columbia, supported by Life Sciences Institute, the UBC GREx Biological Resilience Initiative.

REFERENCES

(1) Leal Filho, W.; Saari, U.; Fedoruk, M.; Iital, A.; Moora, H.; Klöga, M.; Voronova, V. An Overview of the Problems Posed by Plastic Products and the Role of Extended Producer Responsibility in Europe. Journal of Cleaner Production 2019, 214, 550–558. https://doi.org/10.1016/j.jclepro.2018.12.256.

(2) Rosenboom, J.-G.; Langer, R.; Traverso, G. Bioplastics for a Circular Economy. Nat Rev Mater 2022, 7 (2), 117–137. https://doi.org/10.1038/s41578-021-00407-8.

(3) Sohn, Y. J.; Kim, H. T.; Baritugo, K.-A.; Jo, S. Y.; Song, H. M.; Park, S. Y.; Park, S. K.; Pyo, J.; Cha, H. G.; Kim, H.; Na, J.-G.; Park, C.; Choi, J.-I.; Joo, J. C.; Park, S. J. Recent Advances in Sustainable Plastic Upcycling and Biopolymers. Biotechnology Journal 2020, 15 (6), 1900489. https://doi.org/10.1002/biot.201900489.

(4) Andrady, A. L.; Barnes, P. W.; Bornman, J. F.; Gouin, T.; Madronich, S.; White, C. C.; Zepp, R. G.; Jansen, M. A. K. Oxidation and Fragmentation of Plastics in a Changing Environment; from UV-Radiation to Biological Degradation. Science of The Total Environment 2022, 851, 158022. https://doi.org/10.1016/j.scitotenv.2022.158022.

(5) Wang, J.; Sun, C.; Huang, Q.-X.; Chi, Y.; Yan, J.-H. Adsorption and Thermal Degradation of Microplastics from Aqueous Solutions by Mg/Zn Modified Magnetic Biochars. Journal of Hazardous Materials 2021, 419, 126486. https://doi.org/10.1016/j.jhazmat.2021.126486.

(6) Winkler, A.; Santo, N.; Ortenzi, M. A.; Bolzoni, E.; Bacchetta, R.; Tremolada, P. Does Mechanical Stress Cause Microplastic Release from Plastic Water Bottles? Water Research 2019, 166, 115082. https://doi.org/10.1016/j.watres.2019.115082.

(7) Urso, M.; Ussia, M.; Novotný, F.; Pumera, M. Trapping and Detecting Nanoplastics by MXene-Derived Oxide Microrobots. Nat Commun 2022, 13 (1), 3573. https://doi.org/10.1038/s41467-022-31161-2.

(8) Shen, M.; Zhang, Y.; Zhu, Y.; Song, B.; Zeng, G.; Hu, D.; Wen, X.; Ren, X. Recent Advances in Toxicological Research of Nanoplastics in the Environment: A Review. Environmental Pollution 2019, 252, 511–521. https://doi.org/10.1016/j.envpol.2019.05.102.

(9) Vethaak, A. D.; Legler, J. Microplastics and Human Health. Science 2021, 371 (6530), 672–674. https://doi.org/10.1126/science.abe5041.

(10) Schmid, T.; Opilik, L.; Blum, C.; Zenobi, R. Nanoscale Chemical Imaging Using Tip-Enhanced Raman Spectroscopy: A Critical Review. Angewandte Chemie International Edition 2013, 52 (23), 5940–5954. https://doi.org/10.1002/anie.201203849.

(11) Schwaferts, C.; Niessner, R.; Elsner, M.; Ivleva, N. P. Methods for the Analysis of Submicrometer- and Nanoplastic Particles in the Environment. TrAC Trends in Analytical Chemistry 2019, 112, 52–65. https://doi.org/10.1016/j.trac.2018.12.014.

(12) Liang, Y.; Hu, S.; Zhang, Q.; Zhang, D.; Guo, G.; Wang, X. Determination of Nanoplastics Using a Novel Contactless Conductivity Detector with Controllable Geometric Parameters. Anal. Chem. 2022, 94 (3), 1552–1558. https://doi.org/10.1021/acs.analchem.1c02752.

(13) Zhou, X.-X.; He, S.; Gao, Y.; Li, Z.-C.; Chi, H.-Y.; Li, C.-J.; Wang, D.-J.; Yan, B. Protein Corona-Mediated Extraction for Quantitative Analysis of Nanoplastics in Environmental Waters by Pyrolysis Gas Chromatography/Mass Spectrometry. Anal. Chem. 2021, 93 (17), 6698–6705. https://doi.org/10.1021/acs.analchem.1c00156.

(14) Zangmeister, C. D.; Radney, J. G.; Benkstein, K. D.; Kalanyan, B. Common Single-Use Consumer Plastic Products Release Trillions of Sub-100 Nm Nanoparticles per Liter into Water during Normal Use. Environ. Sci. Technol. 2022, 56 (9), 5448–5455. https://doi.org/10.1021/acs.est.1c06768.

(15) Jiménez-Lamana, J.; Marigliano, L.; Allouche, J.; Grassl, B.; Szpunar, J.; Reynaud, S. A Novel Strategy for the Detection and Quantification of Nanoplastics by Single Particle Inductively Coupled Plasma Mass Spectrometry (ICP-MS). Anal. Chem. 2020, 92 (17), 11664–11672. https://doi.org/10.1021/acs.analchem.0c01536.

(16) Xu, Y.; Ou, Q.; Jiao, M.; Liu, G.; van der Hoek, J. P. Identification and Quantification of Nanoplastics in Surface Water and Groundwater by Pyrolysis Gas Chromatography–Mass Spectrometry. Environ. Sci. Technol. 2022, 56 (8), 4988–4997. https://doi.org/10.1021/acs.est.1c07377.

(17) Leonard, J.; Koydemir, H. C.; Koutnik, V. S.; Tseng, D.; Ozcan, A.; Mohanty, S. K. Smartphone-Enabled Rapid Quantification of Microplastics. Journal of Hazardous Materials Letters 2022, 3, 100052. https://doi.org/10.1016/j.hazl.2022.100052.

(18) Chen, S.-J.; Chang, H.-T. Nile Red-Adsorbed Gold Nanoparticles for Selective Determination of Thiols Based on Energy Transfer and Aggregation. Anal. Chem. 2004, 76 (13), 3727–3734. https://doi.org/10.1021/ac049787s.

(19) Bhangu, S. K.; Charchar, P.; Noble, B. B.; Kim, C.-J.; Pan, S.; Yarovsky, I.; Cavalieri, F.; Caruso, F. Origins of Structural Elasticity in Metal–Phenolic Networks Probed by Super-Resolution Microscopy and Multiscale Simulations. ACS Nano 2022, 16 (1), 98–110. https://doi.org/10.1021/acsnano.1c08192.

(20) Fan, G.; Wasuwanich, P.; Rodriguez-Otero, M. R.; Furst, A. L. Protection of Anaerobic Microbes from Processing Stressors Using Metal–Phenolic Networks. J. Am. Chem. Soc. 2022, 144 (6), 2438–2443. https://doi.org/10.1021/jacs.1c09018.

(21) Kim, C.-J.; Ercole, F.; Chen, J.; Pan, S.; Ju, Y.; Quinn, J. F.; Caruso, F. Macromolecular Engineering of Thermoresponsive Metal–Phenolic Networks. J. Am. Chem. Soc. 2022, 144 (1), 503–514. https://doi.org/10.1021/jacs.1c10979.

(22) Lin, Z.; Zhou, J.; Qu, Y.; Pan, S.; Han, Y.; Lafleur, R. P. M.; Chen, J.; Cortez-Jugo, C.; Richardson, J. J.; Caruso, F. Luminescent Metal-Phenolic Networks for Multicolor Particle Labeling. Angewandte Chemie International Edition 2021, 60 (47), 24968–24975. https://doi.org/10.1002/anie.202108671.

(23) Lin, Z.; Zhou, J.; Qu, Y.; Pan, S.; Han, Y.; Lafleur, R. P. M.; Chen, J.; Cortez-Jugo, C.; Richardson, J. J.; Caruso, F. Luminescent Metal-Phenolic Networks for Multicolor Particle Labeling. Angew. Chem. 2021, 133 (47), 25172–25179. https://doi.org/10.1002/ange.202108671.

(24) Kowal, M.; Seifried, T.; Brouwer, C.; Tavakolizadeh, H.; Grant, E. EPD-iSCAT: Electrophoretic Mass Photometry. ChemRxiv October 25, 2023. https://doi.org/10.26434/chemrxiv-2023-ddzfc.

(25) Cai, H.; Xu, E. G.; Du, F.; Li, R.; Liu, J.; Shi, H. Analysis of Environmental Nanoplastics: Progress and Challenges. Chemical Engineering Journal 2021, 410, 128208. https://doi.org/10.1016/j.cej.2020.128208.

(26) Lin, Z.; Zhou, J.; Cortez-Jugo, C.; Han, Y.; Ma, Y.; Pan, S.; Hanssen, E.; Richardson, J. J.; Caruso, F. Ordered Mesoporous Metal–Phenolic Network Particles. J. Am. Chem. Soc. 2020, 142 (1), 335–341. https://doi.org/10.1021/jacs.9b10835.

(27) Rahim, Md. A.; Björnmalm, M.; Bertleff-Zieschang, N.; Besford, Q.; Mettu, S.; Suma, T.; Faria, M.; Caruso, F. Rust-Mediated Continuous Assembly of Metal–Phenolic Networks. Advanced Materials 2017, 29 (22), 1606717. https://doi.org/10.1002/adma.201606717.

(28) Guo, J.; Ping, Y.; Ejima, H.; Alt, K.; Meissner, M.; Richardson, J. J.; Yan, Y.; Peter, K.; von Elverfeldt, D.; Hagemeyer, C. E.; Caruso, F. Engineering Multifunctional Capsules through the Assembly of Metal-Phenolic Networks. Angew. Chem. Int. Ed. 2014, 53 (22), 5546–5551. https://doi.org/10.1002/anie.201311136.

(29) Arbeloa, F. L.; Ojeda, P. R.; Arbeloa, I. L. Flourescence Self-Quenching of the Molecular Forms of Rhodamine B in Aqueous and Ethanolic Solutions. Journal of Luminescence 1989, 44 (1), 105–112. https://doi.org/10.1016/0022-2313(89)90027-6.

(30) Kim, C.-J.; Ercole, F.; Chen, J.; Pan, S.; Ju, Y.; Quinn, J. F.; Caruso, F. Macromolecular Engineering of Thermoresponsive Metal–Phenolic Networks. J. Am. Chem. Soc. 2022, 144 (1), 503–514. https://doi.org/10.1021/jacs.1c10979.

(31) Chen, J.; Pan, S.; Zhou, J.; Seidel, R.; Beyer, S.; Lin, Z.; Richardson, J. J.; Caruso, F. Metal–Phenolic Networks as Tunable Buffering Systems. Chem. Mater. 2021, 33 (7), 2557–2566. https://doi.org/10.1021/acs.chemmater.1c00015.

(32) Xie, L.; Gong, K.; Liu, Y.; Zhang, L. Strategies and Challenges of Identifying Nanoplastics in Environment by Surface-Enhanced Raman Spectroscopy. Environ. Sci. Technol. 2023, 57 (1), 25–43. https://doi.org/10.1021/acs.est.2c07416.

(33) Zhang, W.; Dong, Z.; Zhu, L.; Hou, Y.; Qiu, Y. Direct Observation of the Release of Nanoplastics from Commercially Recycled Plastics with Correlative Raman Imaging and Scanning Electron Microscopy. ACS Nano 2020, 14 (7), 7920–7926. https://doi.org/10.1021/acsnano.0c02878.

Table of contents